Article

Dipolar quantum solids emerging in a Hubbard quantum simulator

https://doi.org/10.1038/s41586-023-06614-3

Received: 14 June 2023

Accepted: 5 September 2023

Published online: 25 October 2023

Check for updates

Lin Su[1]✉, Alexander Douglas[1], Michal Szurek[1], Robin Groth[1], S. Furkan Ozturk[1], Aaron Krahn[1], Anne H. Hébert[1], Gregory A. Phelps[1], Sepehr Ebadi[1], Susannah Dickerson[1], Francesca Ferlaino[2,3], Ognjen Marković[1] & Markus Greiner[1]✉

In quantum mechanical many-body systems, long-range and anisotropic interactions promote rich spatial structure and can lead to quantum frustration, giving rise to a wealth of complex, strongly correlated quantum phases[1]. Long-range interactions play an important role in nature; however, quantum simulations of lattice systems have largely not been able to realize such interactions. A wide range of efforts are underway to explore long-range interacting lattice systems using polar molecules[2–5], Rydberg atoms[2,6–8], optical cavities[9–11] or magnetic atoms[12–15]. Here we realize novel quantum phases in a strongly correlated lattice system with long-range dipolar interactions using ultracold magnetic erbium atoms. As we tune the dipolar interaction to be the dominant energy scale in our system, we observe quantum phase transitions from a superfluid into dipolar quantum solids, which we directly detect using quantum gas microscopy with accordion lattices. Controlling the interaction anisotropy by orienting the dipoles enables us to realize a variety of stripe-ordered states. Furthermore, by transitioning non-adiabatically through the strongly correlated regime, we observe the emergence of a range of metastable stripe-ordered states. This work demonstrates that novel strongly correlated quantum phases can be realized using long-range dipolar interactions in optical lattices, opening the door to quantum simulations of a wide range of lattice models with long-range and anisotropic interactions.

Quantum simulations[16] with ultracold atoms in optical lattices enable the exploration of strongly correlated quantum matter described by the Hubbard model[17] and are reaching regimes that are extremely challenging to access numerically[18]. Quantum simulations of the Hubbard model, however, have so far largely been limited to local on-site interactions, and it has been a long-standing goal to realize simulations with strong long-range interactions. This would allow the quantum simulation of models that more accurately describe realistic quantum materials like transition metal dichalcogenides, which typically experience finite off-site Coulomb repulsion[19]. Tunable anisotropic long-range interactions would furthermore open the door to modelling quantum materials such as spin ice[20], anisotropic materials[21] and twisted bilayer materials[22], as well as a wide range of models beyond current quantum material realizations. Long-range interactions naturally promote spatial structure, leading to the emergence of solid phases. In stark contrast to short-range Hubbard models, long-range interactions can lead to frustration in otherwise non-frustrated geometries, hosting supersolids[23–27], spin liquids[28] and fractionalization[29]. Generally, a fundamental question arises about how do long-range interactions compete with kinetic energy and on-site interactions to give rise to novel quantum phases of matter.

Developing approaches for realizing long-range interacting systems and addressing this question is an exceptionally active field of research. Significant progress has been made to create controllable systems of cold polar molecules[2,5], with ongoing efforts towards itinerant lattice gases[3,4]. Rydberg interactions have enabled the quantum simulations of programmable Ising and XY spin models[2,6,7]. However, using Rydberg dressing to realize itinerant models[8] presents challenges due to Rydberg decay. Dynamic light fields in optical cavities enable the study of infinite-range[9,10] and finite-range[11] interacting atom systems, with dissipation being the main hurdle for reaching strongly correlated lattice physics. Furthermore, recent experiments in condensed matter systems have simulated long-range interacting Hubbard systems with bulk measurements[30–32]; yet, it is challenging to perform site-resolved studies in these simulators.

Magnetic atoms provide an attractive alternative to the systems mentioned above, as they are relatively simple to control and interact through the long-range magnetic dipole–dipole interaction[33]. In bulk systems, the atoms collectively order in the presence of a magnetic interaction, leading to intriguing effects such as macroscopic dipolar droplets forming a supersolid phase[12]. To realize strongly correlated physics, however, the long-range interaction energy between pairs of individual atoms needs to become large compared to the kinetic energy[34]. It has been shown that a small-spacing optical lattice of magnetic atoms leads to a Hubbard system with dipolar interactions large enough to cause a notable shift of the superfluid to Mott insulator

[1]Department of Physics, Harvard University, Cambridge, MA, USA. [2]Institut für Experimentalphysik, Universität Innsbruck, Innsbruck, Austria. [3]Institut für Quantenoptik und Quanteninformation, Österreichische Akademie der Wissenschaften, Innsbruck, Austria. ✉e-mail: lin_su@g.harvard.edu; greiner@physics.harvard.edu

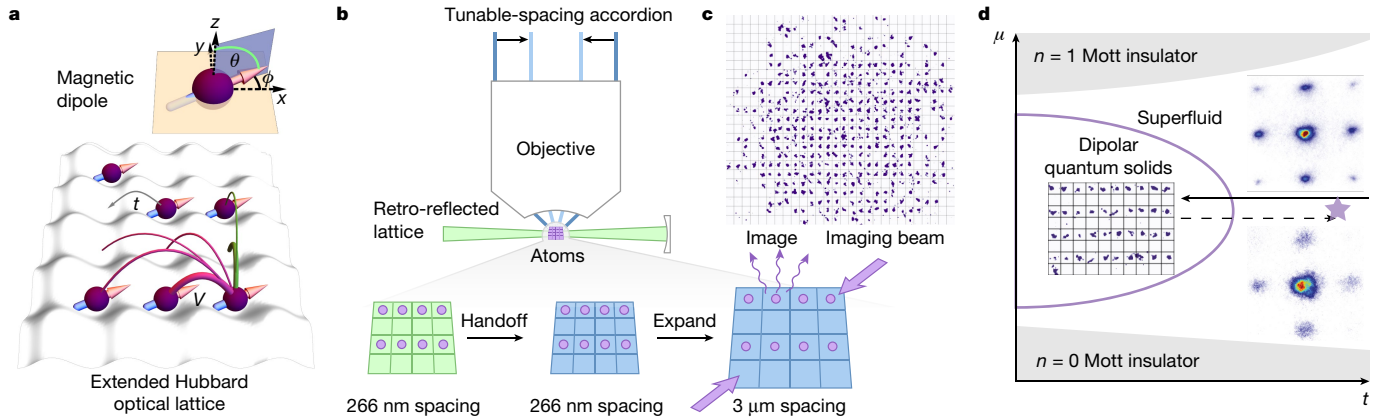

Fig. 1 | Experimental set-up. Magnetic erbium atoms in an optical lattice realize an extended Hubbard model with anisotropic long-range interactions, thus enabling the realization of novel strongly correlated quantum phases. **a**, Orienting the magnetic dipoles using an external magnetic field allows us to widely tune the anisotropy of the interaction, with θ being the polar angle, ϕ the azimuthal angle, the pink (green) lines denoting attractive (repulsive) dipole–dipole interaction V and the grey arrow denoting tunnelling t. **b**, We use a small-spacing lattice to maximize the dipolar interaction strength. Quantum gas microscopy is realized by handing off atoms from the small-spacing retro-reflected lattices (green) to tunable-spacing accordion lattices (blue). **c**, After expanding the accordion lattice, fast fluorescence imaging results in site-resolved single-shot images. **d**, Schematic of the extended Bose–Hubbard phase diagram with dipolar interactions. The solid arrow indicates the ramp we perform to induce a quantum phase transition from a strongly correlated superfluid to a half-filling dipolar quantum solid. Insets, an exemplary single-shot image of a solid (same as Fig. 2c) and time-of-flight images taken at the star location before the ramp (top) and after ramping back to the superfluid phase along the dashed arrow (bottom). The persistence of the superfluid matter wave peaks after ramping back from the solid qualitatively demonstrates the adiabaticity of the ramp.

transition[13]. However, whether the intersite dipolar interactions can experimentally be made the dominant energy scale and larger than the kinetic energy and temperature remained an open question. Here, we present an affirmative answer to this question by observing quantum phase transitions from a strongly correlated superfluid to dipolar quantum solids, that is phases of matter that show spontaneous periodic density modulation in the presence of quantum fluctuations due to finite tunnelling. This long-range and anisotropic interaction is expected to give rise to a rich set of states with fractional fillings[24,25,35–38]. In this work, we probe such states at half-filling.

Dipolar quantum gas microscope

We realize the two-dimensional (2D) extended Bose–Hubbard model with anisotropic long-range dipolar interactions by employing magnetic erbium atoms in an optical lattice (Fig. 1a). In this work, we choose the atomic on-site Hubbard repulsion to be much larger than other energy scales. This realizes an extended Hubbard model in the hard-core boson limit in which each lattice site is populated by either zero or one atom (Methods). The Hubbard Hamiltonian of our system is

$$H = -t\sum_{\langle i,j\rangle}(\hat{a}_i^\dagger\hat{a}_j + \text{h.c.}) - \sum_i \mu_i\hat{n}_i + \sum_{i<j} V_{i,j}\hat{n}_i\hat{n}_j. \quad (1)$$

Here, $\hat{a}_i^\dagger\hat{a}_j$ describes the tunnelling of hard-core bosons between nearest-neighbour sites with amplitude t, $\hat{n}_i$ is the number operator on site i and μ_i is the chemical potential on site i. The dipolar interaction between lattice sites i and j with distance $\mathbf{d}_{i,j} = (d_x, d_y)$ sites is $V_{i,j} = V_0\frac{1-3((d_x/d)\sin\theta\cos\phi + (d_y/d)\sin\theta\sin\phi)^2}{d^3}$, where (θ, ϕ) are the dipole polar and azimuthal angles (Fig. 1a), $d = |\mathbf{d}_{i,j}|$ and V_0 is the nearest-neighbour repulsive interaction energy when the dipole is oriented out of the 2D plane ($\theta = 0°$).

The major challenge when observing dipolar quantum solids using magnetic atoms is posed by the relatively weak magnetic interactions between atoms compared to the typical energy scales in quantum simulators. We reach a nearest-neighbour interaction energy of $V_0 \approx h \times 30$ Hz, where h is Planck's constant, by using a small-spacing optical lattice (green beams in Fig. 1b) with $a = 266$ nm lattice spacing[13]. To resolve individual sites in this lattice, we developed a novel quantum gas microscopy technique using a tunable-spacing two-dimensional accordion lattice projected in vacuo through an objective with a high numerical aperture (blue beams in Fig. 1b). For imaging, we transferred atoms from the small-spacing lattice to the accordion lattice and then expanded the spacing of the accordion lattice. Finally, we imaged with single-site resolution (Methods); a snapshot of a Mott insulator is shown in Fig. 1c.

The dipolar interaction strength is nearly four orders of magnitude smaller than the optical lattice depth; hence, it is essential to minimize the lattice disorder that causes the disorder in the chemical potential μ_i. We reduced the potential disorder to within a fraction of V_0 by minimizing the scattered light intensity in the atom plane and ensuring that the residual disorder length scale is large. This was done by making sure that all optical surfaces on which lattice beams were incident were at least a few Rayleigh ranges away from the atomic plane[39]. This necessitates a custom objective with a central bore to minimize scattering of the vertical lattice beam (Methods).

For the experiment, we started with a Bose–Einstein condensate of ^{168}Er created in less than 1 s using narrow line laser cooling[40]. We then loaded the atoms into a single layer of a retro-reflected vertical lattice (Methods). We robustly loaded sufficient atoms into the lattice to reach around 100 atoms on 200 sites in the central region of interest. The atomic dipole direction was set by aligning the dipoles to a tunable external magnetic field that was static during the lattice ramp. The small-spacing lattice power was ramped adiabatically to reach the target lattice depth following the solid arrow in Fig. 1d, such that we achieved $t/V_0 \approx 0.1$. Remarkably, we were able to ensure that the process was adiabatic down to low tunnelling strengths, corresponding to adiabatic cooling[41] to temperatures (T) of only several hundred picokelvin ($k_BT/V_0 \approx 0.5$, where k_B is the Boltzmann constant). For imaging, we rapidly increased the lattice depth to turn off the tunnelling in the small-spacing lattice and projected the state of the system into the occupation basis. We then handed off the atoms to the accordion lattice and expanded the lattice spacing to 3 μm. The lattice dynamics were kept frozen when expanding the accordion lattice spacing such

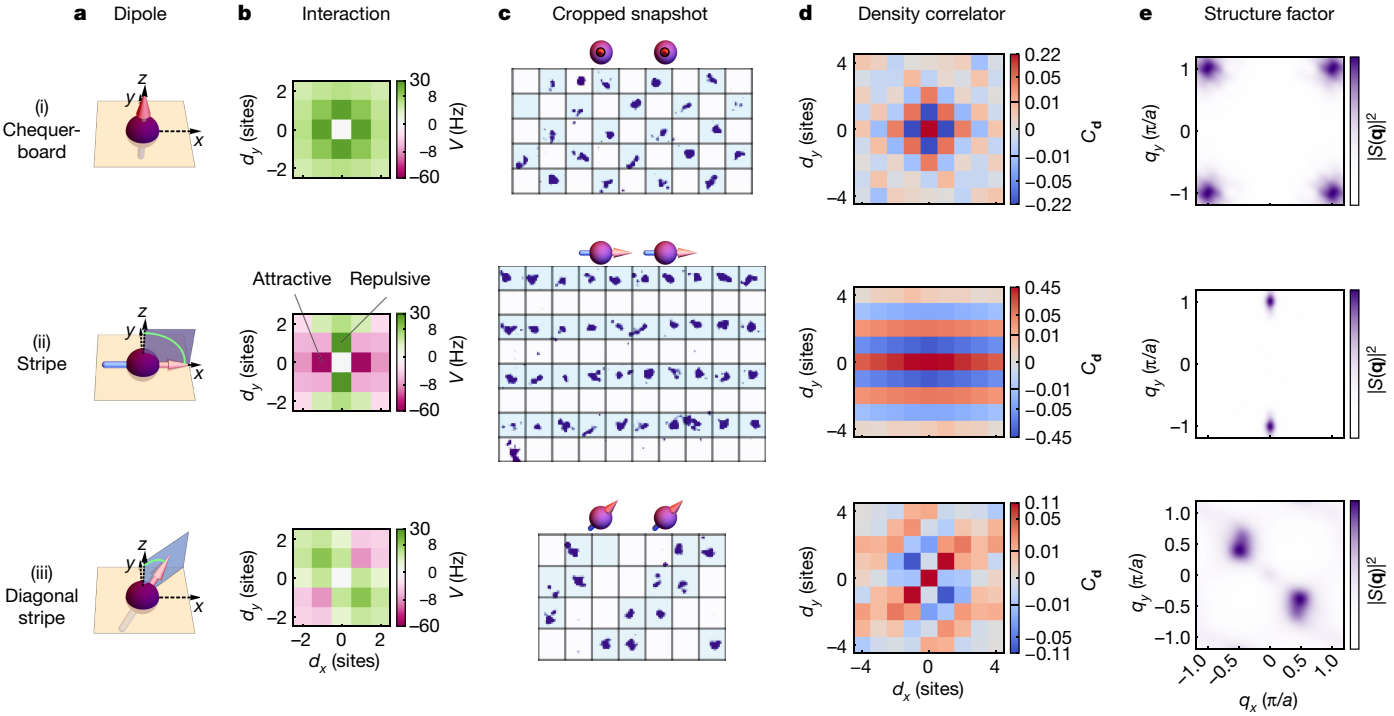

Fig. 2 | Dipolar quantum solids. As the dipolar interaction V_0 becomes dominant over tunnelling t, dipolar quantum solids emerge. **a**,**b**, In row (i), dipoles pointing in the z direction (**a**) give rise to isotropic $1/d^3$ repulsion (**b**). **c**, An exemplary single-shot image shows the chequerboard solid arising at half-filling (blue shading to guide the eye). **d**, The emerging order can be analysed quantitatively by calculating the connected density–density correlator $C_{\mathbf{d}}$ averaged over experimental realizations, with a linear colour bar between −0.01 and 0.01 and logarithmic elsewhere. **e**, A Fourier transform of $C_{\mathbf{d}}$ yields the structure factor $S(\mathbf{q})$, whose magnitude squared is plotted with a linear colour bar starting from zero. With the dipole aligned in the x direction (row (ii)), the interaction becomes highly anisotropic, and the atoms form a stripe solid. For diagonally aligned dipoles (row (iii)) (here, $\theta = 50°$ and $\phi = 45°$), we observe diagonally ordered states. Remarkably, the transition into the diagonal stripe solid is entirely driven by beyond-nearest-neighbour interaction terms.

that the imaged lattice occupation faithfully represented the state of the atoms in the small-spacing lattice (Methods). We then performed fluorescence imaging by exposing the atoms to resonant highly saturated light for 8 μs (ref. 42). A few hundred fluorescence photons per atom were scattered and collected by the objective (Fig. 1b). About 50 photons per atom were detected by the electron-multiplying charge-coupled device (CCD) camera, forming an image from which we extracted the atom occupation number per lattice site. The total experiment cycle time was 2.5 s.

Dipolar quantum solids

We observed the atoms self-organize into different dipolar quantum solids when the dipole–dipole interactions became the dominant energy scale in our system (Fig. 2). These periodically ordered states arose after quantum phase transitions from a strongly correlated superfluid into a dipolar quantum solid, with possible intermediate phases that will be the focus of future work. We transitioned into the solid by adiabatically reducing the kinetic energy of the atoms in the lattice using a linear ramp of lattice depth. The periodic ordering, which is distinct from the periodicity of the lattice, was a signature that the underlying lattice symmetry was broken. By tuning the orientation of the dipoles with the external magnetic field, we realized a wide variety of isotropic and anisotropic interactions, leading to phases with different periodic ordering depending on the dipole orientation (Fig. 2, rows (i), (ii) and (iii)). We analysed the quantum solids directly from single-shot images or by calculating the connected density–density correlation:

$$C_{\mathbf{d}} = \frac{4}{N_{\mathbf{d}}} \sum_{\mathbf{d}=\mathbf{d}_{i,j}} (\langle \hat{n}_i \hat{n}_j \rangle - \langle \hat{n}_i \rangle \langle \hat{n}_j \rangle), \tag{2}$$

where we sum over $N_{\mathbf{d}}$ pairs of lattice sites at distance vector $\mathbf{d}$ in the analysis region and average over hundreds of experimental realizations[43]. Such a correlation shows strong periodic patterns depending on the specific quantum solid (Fig. 2d). The Fourier transform of the correlation (the structure factor)

$$S(\mathbf{q}) \propto \sum_{\mathbf{d}} e^{i\mathbf{q}\cdot\mathbf{d}} C_{\mathbf{d}}, \tag{3}$$

($\mathbf{q}$ is the quasi-momentum) exhibits peaks at positions set by the periodicity of the quantum solid state (Fig. 2e).

Chequerboard solid

First, we tuned the dipole orientation to explore isotropic long-range repulsion. When the atomic dipoles pointed perpendicular to the plane, that is $\theta = 0°$ (Fig. 2a(i)), the atoms isotropically repelled each other with a strength that decays as $1/d^3$, where d is the distance between two lattice sites (Fig. 2b(i)). At half-filling and weak tunnelling, the atoms arranged themselves in the energetically favoured chequerboard pattern. In Fig. 2c(i), we show a chequerboard in a cropped region of an example single-shot image. The periodic chequerboard structure in the observed density correlation (Fig. 2d(i)) and the structure factor exhibiting $(\pm\pi/a, \pm\pi/a)$ peaks (Fig. 2e(i)) is a hallmark of lattice symmetry breaking in a solid[23].

Stripe solid

Next, we maximized the interaction anisotropy between the two lattice axes by orienting the atomic dipoles in the 2D atom plane along

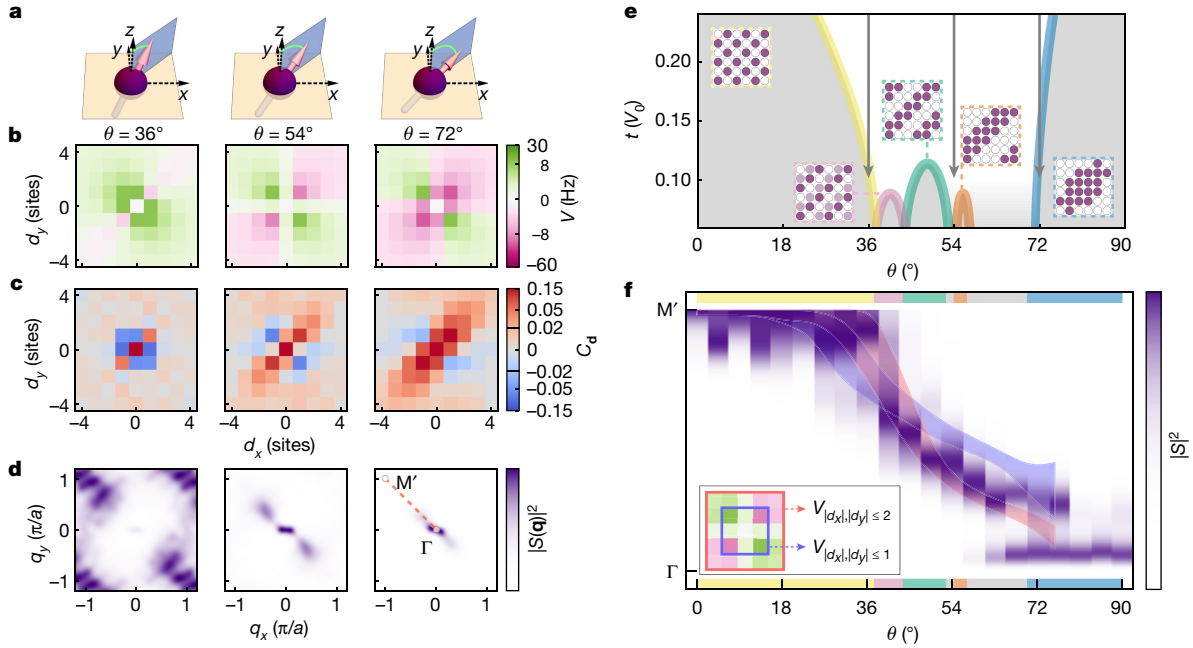

Fig. 3 | Solids and global phase separation with spatial anisotropy. For dipoles aligned diagonally with respect to the lattice vectors ($\phi = 45°$), different polar angles θ give rise to stripe solids with different periodicity. **a**, Dipole orientation with the polar angle highlighted in green. **b**, Anisotropic long-range dipolar interaction energy. **c**, Measured connected density–density correlation. **d**, Magnitude-squared structure factors. **e**, Quantum Monte Carlo simulation of emerging phases. Grey shading indicates solids and white indicates a superfluid region. Each colour border represents a different solid with the ordering shown in the inset. Between 53° and 72°, there are more solid phases without their boundaries marked out in colour. Our adiabatic paths follow the grey arrows. **f**, Experimental structure factor along the orange diagonal line from marker Γ to M′ shown in the rightmost subfigure of **d**, whose coordinates are $(q_x, -q_x)$. Shaded areas show the quantum Monte Carlo simulation results with one standard deviation error. The blue area is a simulation including only nearest-neighbour and diagonal next-nearest-neighbour interaction terms ($|d_x|, |d_y| \leq 1$). The red area includes beyond-next-nearest-neighbour interaction terms ($|d_x|, |d_y| \leq 2$). The experimental data agree better with the latter, indicating that long-range tails beyond-next-nearest-neighbour terms play a significant role in our system.

one of the lattice directions, that is $(\theta, \phi) = (90°, 0°)$ (Fig. 2a(ii)). We observed in single-shot images long chains of atoms aligned with the atomic dipole direction, with an example cropped image shown in Fig. 2c(ii). The phase of the chains changed from shot to shot (Methods), showing the characteristics of spontaneous symmetry breaking. The extracted connected density–density correlation had a periodic stripe pattern (Fig. 2d(ii)) and the density structure factor (Fig. 2e(ii)) clearly exhibited $(0, \pm\pi/a)$ peaks.

Furthermore, we probed the adiabaticity of the transition from the superfluid to dipolar quantum solids by measuring the superfluid coherence peaks before and after the lattice ramp. The superfluid fraction was qualitatively estimated by observing coherence peaks in time-of-flight images, after releasing atoms from the lattice[44]. The inset in Fig. 1d above the solid arrow is a time-of-flight image before ramping into the stripe solid and shows the superfluid coherence peaks, demonstrating the quantum coherence of our initial state. To demonstrate that the ramp into the ordered state was nearly adiabatic, we performed a closed path in parameter space and ramped back into the superfluid phase following the dashed arrow shown in Fig. 1d. We qualitatively checked the return fidelity with the time-of-flight image shown below the dashed arrow. The appearance of interference peaks indicates that ramp to the solid was close to adiabatic.

Diagonal stripe solid

To probe the long-range nature of the dipole–dipole interaction, we aligned the atomic dipole out of the lattice plane along the $(\theta, \phi) = (50°, 45°)$ direction. If our interactions included only nearest-neighbour interactions, this dipole orientation with repulsive nearest-neighbour interactions (Fig. 2b(iii)) would be like the first case with $\theta = 0°$ (Fig. 2b(i)), where we observe the chequerboard solid. In contrast to the chequerboard case, the dipolar interactions beyond nearest neighbours showed a diagonal attraction along one lattice diagonal and repulsion along the other. These interactions gave rise to a ground state of diagonal stripes with a period of $2\sqrt{2}\,a$, as shown in Fig. 2c,d(iii) with a corresponding peak in the structure factor at $\pm(\pi/2, -\pi/2)$ shown in Fig. 2e(iii). The observation of this diagonal stripe solid not only demonstrates the long-range dipolar nature of our interactions but also highlights the low disorder of the local chemical potential μ_i and the low temperature of our system compared to the maximum interaction energy of only $h \times 10$ Hz with this dipole orientation.

The example solid in Fig. 2(iii) demonstrates that aligning the dipole orientation to an azimuthal angle $\phi = 45°$ between the x and y axes can result in an isotropic nearest-neighbour interaction but an anisotropic next-nearest-neighbour interaction, leading to translation symmetry breaking into a large unit cell[45]. Here, we further explored the ordering of the system at low temperature for different polar angles θ (Fig. 3a). We adiabatically reduced the tunnelling and approached the ground state with $t/V_0 \approx 0.1$ at different polar angles θ with the same $\phi = 45°$ (Fig. 3a). As θ (green arc in Fig. 3a) increased, the observed periodicity of the diagonal stripe increased (Fig. 3c) and the structure factor peak (Fig. 3d) moved closer to the origin, indicating a larger unit cell. To gain theoretical understanding, we performed quantum Monte Carlo simulations (Methods) and identified the emerging phases for the experimental parameters in Fig. 3e.

To compare the observed structure factor with the results of quantum Monte Carlo simulations, we plotted the measured density structure factors $S(\mathbf{q})$ along the straight line from point Γ to point M′ in the Brillouin zone (the dotted diagonal line shown in the rightmost subfigure of Fig. 3d), whose coordinates are $(q_x, -q_x)$, and we plotted

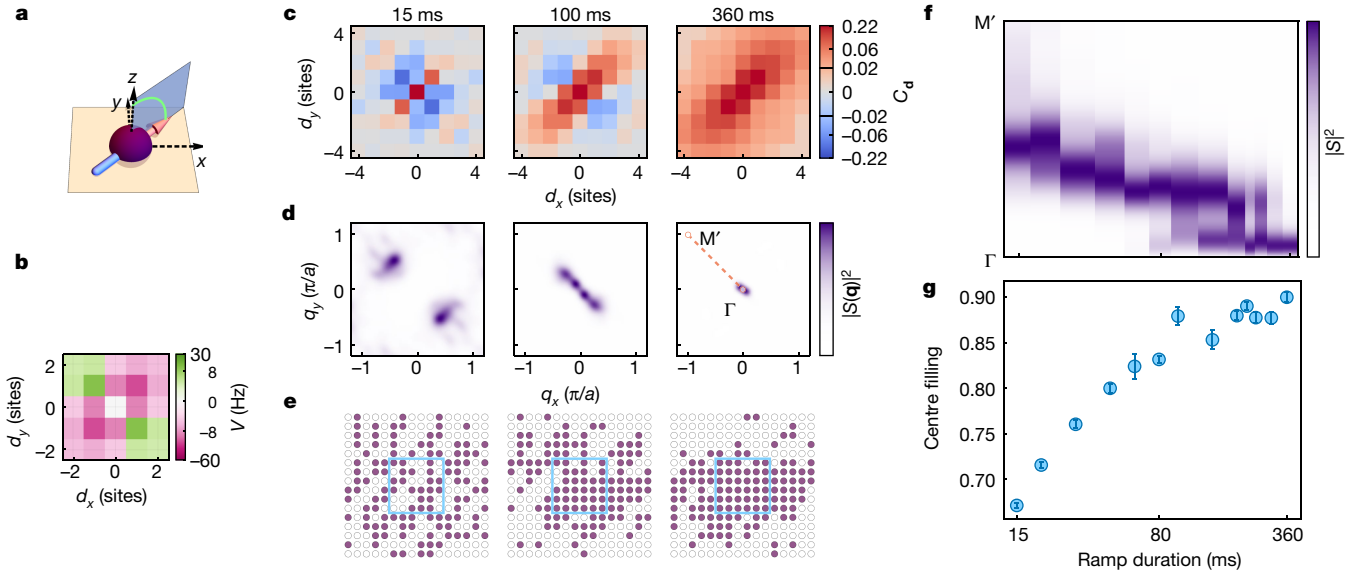

Fig. 4 | Out-of-equilibrium dynamics. After ramping non-adiabatically into the global phase separation state, we observe diagonal stripe solids with different periodicities depending on the ramp speed, which demonstrates the rich manifold of metastable states lying above the global phase separation state. **a**,**b**, The dipole is oriented diagonally in the x–y plane at $\phi = 45°$ and $\theta = 90°$ (**a**), leading to the anisotropic dipolar interaction energy (**b**). **c**–**e**, The connected density–density correlation (**c**), the structure factor (**d**) and single-shot images (**e**) show the various periodicities for different ramp durations of 15 ms, 100 ms and 360 ms. **f**,**g**, We plot the diagonal structure factor (**f**) and the centre (within the blue box in **e**) filling ratio (**g**) to show the emerging phase separation as the filling at the centre approaches unity (the error bars denote the standard error of the mean).

the results in Fig. 3f in increments of 4.5°. The structure factor indicates that there was chequerboard order between $\theta = 0°$ and $\theta \approx 30°$. Then, the peak location of the density structure factor was gradually moved towards the origin until $\theta \approx 80°$. At this point, the attractive long-range interaction dominated over the repulsive one. We observed that the ground state of our finite system was no longer a diagonal stripe solid, but instead, it was a self-organized state with the lattice separated into unity-filled and empty regions, each occupying only half of the sites in the region of interest. We denoted this as a global phase separation state, where the unity-filled region was a self-bound insulator. This state is fundamentally distinct from a unity-filled Mott insulator, as the system would form a half-filling superfluid in the absence of dipolar interactions.

The various types of diagonal stripes that can form between the chequerboard solid and the global phase separation state exemplify the long range of the dipolar interactions beyond next nearest neighbours. We simulated the dipolar interaction cutoff with $|d_x|, |d_y| \leq 1$ (Fig. 3f, blue shade, 3 by 3 box, includes interactions only for the nearest neighbour and the next nearest neighbour) and $|d_x|, |d_y| \leq 2$ (Fig. 3f, red shade, 5 by 5 box, includes interactions beyond next nearest neighbour). The tail of the long-range interactions plays an important role in the self-organization of stripe solids with long periodicity when θ is between 50° and 70°, causing the significant difference between the simulation results with different cutoff ranges. Remarkably, we observed that our data agree with the simulation results, including beyond-next-nearest-neighbour interactions (red shade), highlighting the important role of long-range interaction terms.

Out-of-equilibrium dynamics

We explored the rich out-of-equilibrium physics that emerges from the dipolar interactions (Fig. 4). In particular, the global phase separation state when $(\theta, \phi) = (90°, 45°)$ exhibited a variety of low-lying metastable states, which is a characteristic of long-range interacting systems[46,47]. To explore these metastable states, we dynamically ramped the system starting from a half-filling superfluid using a linear ramp of lattice depth, resulting in an exponential ramp in tunnelling energy from $h \times 300$ Hz to $h \times 3$ Hz. By varying the ramp time, we observed diagonal stripes with different periodicities (Fig. 4c). When the ramp was faster than 100 ms, the structure factor had a signature of diagonal stripes, and the atoms were sparsely arranged throughout the analysis region (Fig. 4e, left). These diagonal stripes were among the lowest-lying metastable states because the dipolar interaction (Fig. 4b) strongly biases diagonal stripes aligned with the dipole direction. As the ramp became more adiabatic, the structure factor peaks migrated towards the origin (Fig. 4f) until they became limited by the system size, and the atoms formed a state that was close to unity-filled (Fig. 4e, right). Due to the finite temperature, we still observed sporadic excitations from the ground state in the form of a missing atom in the centre of the cloud. These excitations did not exhibit a significant spatial structure, unlike the metastable diagonal stripe patterns. Overall, the long-range nature of the dipolar interaction was responsible for the rich out-of-equilibrium physics observed in this system.

Conclusion and outlook

We observed various dipolar quantum solids and global phase separation using ultracold atoms with single-site resolution, finding rich phases caused by the anisotropic long-range dipolar interactions. We found evidence of metastable states, which we accessed by changing the ramp speed across the phase transition from superfluid to the global phase separation state. These observations mark the beginning of studying itinerant, strongly correlated quantum phases originating from dipolar interactions. The dipolar quantum gas microscope is a flexible platform for examining a host of quantum phase transitions between different states in the dipolar system and dynamics across such transitions, such as first-order phase transitions and transitions exhibiting intermediate 'microemulsion' phases[36,48]. Furthermore, metastable states represent an exciting frontier in many-body quantum systems and open the gate to quantum orders not stable in equilibrium[49]. Moreover, going beyond the hard-core boson limit and allowing multiple particles to occupy the same site allows supersolid phases to occupy a much larger region in the phase diagram[50,51] and gives rise to Haldane insulators in one dimension[52]. Leveraging the anisotropic long-range

interactions in this system will allow spin liquids[28] and fractionalization[29] to be examined. Finally, employing fermionic species of magnetic atoms will enable the realization of extended Fermi–Hubbard models in the study of spinful itinerant systems with dipolar interactions, which can show a wide variety of phenomena including bond order waves[53] and ultralong-range order[54].

Online content

Any methods, additional references, Nature Portfolio reporting summaries, source data, extended data, supplementary information, acknowledgements, peer review information; details of author contributions and competing interests; and statements of data and code availability are available at https://doi.org/10.1038/s41586-023-06614-3.

1. Defenu, N. et al. Long-range interacting quantum systems. *Rev. Mod. Phys.* **95**, 035002 (2023).
2. Kaufman, A. M. & Ni, K.-K. Quantum science with optical tweezer arrays of ultracold atoms and molecules. *Nat. Phys.* **17**, 1324–1333 (2021).
3. Rosenberg, J. S., Christakis, L., Guardado-Sanchez, E., Yan, Z. Z. & Bakr, W. S. Observation of the Hanbury Brown-Twiss effect with ultracold molecules. *Nat. Phys.* **18**, 1062–1066 (2022).
4. Li, J.-R. et al. Tunable itinerant spin dynamics with polar molecules. *Nature* **614**, 70–74 (2023).
5. Schindewolf, A. et al. Evaporation of microwave-shielded polar molecules to quantum degeneracy. *Nature* **607**, 677–681 (2022).
6. Chen, C. et al. Continuous symmetry breaking in a two-dimensional Rydberg array. *Nature* **616**, 691–695 (2023).
7. Ebadi, S. et al. Quantum phases of matter on a 256-atom programmable quantum simulator. *Nature* **595**, 227–232 (2021).
8. Guardado-Sanchez, E. et al. Quench dynamics of a Fermi gas with strong nonlocal interactions. *Phys. Rev. X* **11**, 021036 (2021).
9. Mivehvar, F., Piazza, F., Donner, T. & Ritsch, H. Cavity QED with quantum gases: new paradigms in many-body physics. *Adv. Phys.* **70**, 1–153 (2021).
10. Landig, R. et al. Quantum phases from competing short- and long-range interactions in an optical lattice. *Nature* **532**, 476–479 (2016).
11. Guo, Y. et al. An optical lattice with sound. *Nature* **599**, 211–215 (2021).
12. Chomaz, L. et al. Dipolar physics: a review of experiments with magnetic quantum gases. *Rep. Prog. Phys.* **86**, 026401 (2022).
13. Baier, S. et al. Extended Bose–Hubbard models with ultracold magnetic atoms. *Science* **352**, 201–205 (2016).
14. Patscheider, A. et al. Controlling dipolar exchange interactions in a dense three-dimensional array of large-spin fermions. *Phys. Rev. Res.* **2**, 023050 (2020).
15. Lepoutre, S. et al. Out-of-equilibrium quantum magnetism and thermalization in a spin-3 many-body dipolar lattice system. *Nat. Commun.* **10**, 1714 (2019).
16. Altman, E. et al. Quantum simulators: architectures and opportunities. *PRX Quantum* **2**, 017003 (2021).
17. Gross, C. & Bloch, I. Quantum simulations with ultracold atoms in optical lattices. *Science* **357**, 995–1001 (2017).
18. Bohrdt, A., Homeier, L., Reinmoser, C., Demler, E. & Grusdt, F. Exploration of doped quantum magnets with ultracold atoms. *Ann. Phys.* **435**, 168651 (2021).
19. Mak, K. F. & Shan, J. Semiconductor moiré materials. *Nat. Nanotechnol.* **17**, 686–695 (2022).
20. Castelnovo, C., Moessner, R. & Sondhi, S. L. Spin ice, fractionalization, and topological order. *Annu. Rev. Condens. Matter Phys.* **3**, 35–55 (2012).
21. Li, L. et al. Emerging in-plane anisotropic two-dimensional materials. *InfoMat* **1**, 54–73 (2019).
22. Andrei, E. Y. & MacDonald, A. H. Graphene bilayers with a twist. *Nat. Mater.* **19**, 1265–1275 (2020).
23. Boninsegni, M. & Prokof'ev, N. V. Colloquium: supersolids: what and where are they? *Rev. Mod. Phys.* **84**, 759–776 (2012).
24. Wu, H.-K. & Tu, W.-L. Competing quantum phases of hard-core bosons with tilted dipole–dipole interaction. *Phys. Rev. A* **102**, 053306 (2020).
25. Capogrosso-Sansone, B., Trefzger, C., Lewenstein, M., Zoller, P. & Pupillo, G. Quantum phases of cold polar molecules in 2D optical lattices. *Phys. Rev. Lett.* **104**, 125301 (2010).
26. Bruder, C., Fazio, R. & Schön, G. Superconductor–Mott-insulator transition in Bose systems with finite-range interactions. *Phys. Rev. B* **47**, 342–347 (1993).
27. Batrouni, G. G., Scalettar, R. T., Zimanyi, G. T. & Kampf, A. P. Supersolids in the Bose–Hubbard Hamiltonian. *Phys. Rev. Lett.* **74**, 2527–2530 (1995).
28. Yao, N. Y., Zaletel, M. P., Stamper-Kurn, D. M. & Vishwanath, A. A quantum dipolar spin liquid. *Nat. Phys.* **14**, 405–410 (2018).
29. Mao, D., Zhang, K. & Kim, E.-A. Fractionalization in fractional correlated insulating states at $n \pm 1/3$ filled twisted bilayer graphene. *Phys. Rev. Lett.* **131**, 106801 (2023).
30. Lagoin, C. et al. Extended Bose–Hubbard model with dipolar excitons. *Nature* **609**, 485–489 (2022).
31. Hensgens, T. et al. Quantum simulation of a Fermi–Hubbard model using a semiconductor quantum dot array. *Nature* **548**, 70–73 (2017).
32. Kennes, D. M. et al. Moiré heterostructures as a condensed-matter quantum simulator. *Nat. Phys.* **17**, 155–163 (2021).
33. Lahaye, T., Menotti, C., Santos, L., Lewenstein, M. & Pfau, T. The physics of dipolar bosonic quantum gases. *Rep. Prog. Phys.* **72**, 126401 (2009).
34. Dutta, O. et al. Non-standard Hubbard models in optical lattices: a review. *Rep. Prog. Phys.* **78**, 066001 (2015).
35. Menotti, C., Trefzger, C. & Lewenstein, M. Metastable states of a gas of dipolar bosons in a 2D optical lattice. *Phys. Rev. Lett.* **98**, 235301 (2007).
36. Zhang, C., Safavi-Naini, A., Maria Rey, A. & Capogrosso-Sansone, B. Equilibrium phases of tilted dipolar lattice bosons. *New J. Phys.* **17**, 123014 (2015).
37. Góral, K., Santos, L. & Lewenstein, M. Quantum phases of dipolar bosons in optical lattices. *Phys. Rev. Lett.* **88**, 170406 (2002).
38. Danshita, I. & Sá de Melo, C. A. R. Stability of superfluid and supersolid phases of dipolar bosons in optical lattices. *Phys. Rev. Lett.* **103**, 225301 (2009).
39. Phelps, G. A. *A Dipolar Quantum Gas Microscope*. PhD thesis, Harvard Univ. (2019).
40. Phelps, G. A. et al. Sub-second production of a quantum degenerate gas. Preprint at https://arxiv.org/abs/2007.10807 (2020).
41. Pollet, L., Kollath, C., Van Houcke, K. & Troyer, M. Temperature changes when adiabatically ramping up an optical lattice. *New J. Phys.* **10**, 065001 (2008).
42. Bergschneider, A. et al. Spin-resolved single-atom imaging of ^{6}Li in free space. *Phys. Rev. A* **97**, 063613 (2018).
43. Mazurenko, A. et al. A cold-atom Fermi–Hubbard antiferromagnet. *Nature* **545**, 462–466 (2017).
44. Greiner, M., Mandel, O., Esslinger, T., Hänsch, T. W. & Bloch, I. Quantum phase transition from a superfluid to a Mott insulator in a gas of ultracold atoms. *Nature* **415**, 39–44 (2002).
45. Zhang, J., Zhang, C., Yang, J. & Capogrosso-Sansone, B. Supersolid phases of lattice dipoles tilted in three dimensions. *Phys. Rev. A* **105**, 063302 (2022).
46. Defenu, N. Metastability and discrete spectrum of long-range systems. *Proc. Natl Acad. Sci.* **118**, e2101785118 (2021).
47. Trefzger, C., Menotti, C. & Lewenstein, M. Ultracold dipolar gas in an optical lattice: the fate of metastable states. *Phys. Rev. A* **78**, 043604 (2008).
48. Spivak, B. & Kivelson, S. A. Phases intermediate between a two-dimensional electron liquid and Wigner crystal. *Phys. Rev. B* **70**, 155114 (2004).
49. Sahay, R., Vishwanath, A. & Verresen, R. Quantum spin puddles and lakes: Nisq-era spin liquids from non-equilibrium dynamics. Preprint at https://arxiv.org/abs/2211.01381 (2022).
50. Iskin, M. Route to supersolidity for the extended Bose–Hubbard model. *Phys. Rev. A* **83**, 051606 (2011).
51. Grimmer, D., Safavi-Naini, A., Capogrosso-Sansone, B. & Söyler, Ş. G. Quantum phases of dipolar soft-core bosons. *Phys. Rev. A* **90**, 043635 (2014).
52. Dalla Torre, E. G., Berg, E. & Altman, E. Hidden order in 1D Bose insulators. *Phys. Rev. Lett.* **97**, 260401 (2006).
53. Julià-Farré, S. et al. Revealing the topological nature of the bond order wave in a strongly correlated quantum system. *Phys. Rev. Res.* **4**, L032005 (2022).
54. van Loon, E. G. C. P., Katsnelson, M. I. & Lemeshko, M. Ultralong-range order in the Fermi–Hubbard model with long-range interactions. *Phys. Rev. B* **92**, 081106 (2015).

Methods

Model calibration

We studied the extended Bose–Hubbard model in the hard-core boson limit since the on-site interaction energy U in our system is much larger than the tunnelling energy t, dipolar energy scale V_0 and chemical potential μ_i. Thus, we neglect the on-site interaction term $\frac{U}{2}\sum_i \hat{n}_i(\hat{n}_i - 1)$ in the standard Bose–Hubbard Hamiltonian. We estimated the on-site interaction energy U to be $h \times 1$ kHz to 2 kHz, depending on the atomic dipole orientation. We measured U by modulating the lattice intensity and observing atom loss in the lattice when the modulation frequency was close to U (ref. 13). We also computed U by taking into account the vertical Wannier function width as well as the dipole orientation, finding good agreement with previous measurements[55]. Such high U results in a negligible super-exchange energy of $h \times 0.01$ Hz ($4 \times 10^{-4}\, V_0$) at typical tunnelling energies at which we examine dipolar quantum solids. To calibrate the tunnelling t for the data in this paper, we measured the lattice depth with lattice modulation[13]. From the measured lattice depth, we numerically obtained the lattice band structure and estimated the tunnelling from the ground bandwidth[56]. We computed the density-induced tunnelling[34] to be an order of magnitude smaller than the single-particle tunnelling t, so we neglected the term in the Hamiltonian. The variation of the chemical potential μ_i in our system consisted of the global harmonic confinement introduced by the lattice beams and the site-to-site disorder in the centre of the analysis region. We measured the global harmonic confinement by measuring the oscillation frequency of the atomic cloud after releasing the atoms from a tight dipole trap. We estimated the chemical potential disorder in the analysis region of interest (around 100 sites) by comparing the measured lattice filling to the exact diagonalization simulation. Specifically, we ramped the lattice to different lattice depths and measured the standard deviation of the average atom number filling. We compared this measurement with a simulation of a 4×4 site system by exact diagonalization, assuming that the disorder follows a uniform distribution[57]. We estimated the chemical potential μ_i disorder to be $h \times 3$ Hz from site to site, in addition to a global harmonic confinement. We computed the dipolar interaction strength $V_{i,j}$ at different distances by taking into account the non-zero width of the Wannier function, which can modify the interactions between the nearest-neighbour sites significantly[58].

Lattice stability

At several points in the experimental sequence, we transferred atoms between different sets of lattices, which required a stable relative lattice phase for reliability. To achieve high stability, we used the vacuum chamber as a reference for all the lattices in our experiment. The 2D small-spacing 532-nm-wavelength lattices were retro-reflected from mirrors attached to the vacuum chamber. The 2D tunable-spacing 488-nm-wavelength accordion lattices were sent through the objective, which was directly mounted inside the vacuum chamber. The vertical 1,064-nm-wavelength lattice was retro-reflected from a mirror mounted on top of the in-vacuum objective. To match the phase of the 2D small-spacing retro-reflected lattices to that of the 2D accordion lattices, we used a thin anti-reflection coated window mounted on a galvanometer to tune the path length difference of the accordion beams. Once the system had warmed up for 2 h, the phases of the lattices stayed stable for more than 24 h.

Reducing the local chemical potential disorder

Achieving chemical potential disorder smaller than the dipolar interaction energy scale V_0 means that the intensity of scattered light interfering with the main lattice beam has to be less than 1 part per million—an extraordinarily low ratio to achieve experimentally. We found that the main source of chemical potential disorder in our experiment to be the scattered vertical lattice light. Therefore, we tuned the intensity of the vertical lattice to be as low as possible, while still keeping the atoms in a single layer of the vertical lattice during the experimental sequence[59]. The energy difference due to gravity in adjacent layers of the vertical lattice prevented the resonant tunnelling of atoms. Experimentally, we observed that a vertical lattice depth of around $7\, E_R$ maximized the dipolar quantum solid order, where E_R is the vertical lattice recoil energy. The lifetime of the atoms at such lattice depth was of the order of a second[60]. Thus, our experimental lattice ramps of a few hundred milliseconds were short enough to keep most of the atoms in the lattice.

State preparation

First, we created a Bose–Einstein condensate in less than a second as described in ref. 40. The single-chamber experiment design removes the complexity of transport. Next, we compressed the atoms into a thin sheet using a vertical 532-nm-wavelength accordion lattice that went through an aspheric lens mounted inside the vacuum chamber in 400 ms. Then we transferred the atoms to a single layer of the vertical 1,064-nm-wavelength retro-reflected lattice. We controlled the final number of atoms in the lattice by tuning the power of an additional optical dipole trap as we turned on a magnetic field gradient to pull the rest of the atoms out of the trap. This process took 600 ms. We observed fluctuations in the number of atoms of a few percent (standard deviation) from shot to shot and did not postselect for exact half-filling (except Extended Data Fig. 3). After turning off the field gradient, we rotated the bias magnetic field to the desired orientation. Finally, we ramped up the 2D small-spacing retro-reflected lattice exponentially for 100 ms to $8\, E_R$ and then linearly for a few hundred milliseconds to $27\, E_R$. To demonstrate the adiabaticity of the lattice ramp, we probed the coherence peaks as we changed the duration of the linear ramp (Extended Data Fig. 1).

Imaging procedure

At the end of each experiment, we froze the dynamics in the small-spacing optical lattice by ramping up the lattice power so that the tunnelling changes from roughly $h \times 3$ Hz to $h \times 0.3$ Hz in 100 μs. We then transferred the atoms from the small-spacing lattice to the 2D accordion lattice in 6 ms. Next, we expanded the 2D accordion lattice spacing from 266 nm to 3 μm in 80 ms (ref. 61). We performed fluorescence imaging of the atoms by exposing them to highly saturated 401 nm resonant beams for 8 μs without cooling or trapping[42]. Thanks to the large 30 MHz linewidth of the imaging transition, we detected roughly 50 photoelectrons during the exposure time using an electron-multiplying CCD camera. To minimize the net momentum on the atoms exerted by the imaging beams, we exposed the atoms to two counter-propagating imaging beams. We alternately pulsed the two counter-propagating beams to eliminate the effect of a standing wave created when both beams were applied at the same time[42]. We kept the beam intensity much higher than the saturation intensity I_{sat}, such that the scattering rate and, thus, the average momentum imparted by each beam onto the atoms were stable without the need for closed-loop feedback of the beam power. During imaging, the atoms experienced movement due to stochastic momentum kicks imparted by the spontaneously emitted photons; however, the random walk moved the atoms by less than half the accordion lattice spacing in most cases.

Imaging fidelity

To distinguish between one and zero atoms on each lattice site, we summed the signals of all camera pixels corresponding to the site and then digitized the number of atoms per site with a precalibrated threshold of 20 photoelectrons per site. Extended Data Fig. 2a is a histogram of the total photoelectron counts of the same site in 9,000 shots collected over 10 h. The two Gaussian-like peaks are well separated and correspond to a fidelity to distinguish between zero and one atom above 99%. Characterizing the loss during the imaging protocol,

including the loss during the transfer into the blue accordion lattice as well as during the expansion of the blue accordion lattice, was more challenging. We prepared a Mott insulator with one particle per site ($n = 1$) and estimated an upper bound of the loss by assuming that the Mott insulator we made has 100% fidelity. Extended Data Fig. 2b is a histogram of the total photoelectron counts within all lattice sites in the centre 10 by 10 sites. We detected the filling of the Mott insulator to be higher than 98%, giving us an upper bound for the loss of 2%.

Numerical simulations

We performed worm-type quantum Monte Carlo simulations based on an existing package[62], which we modified to include long-range dipolar interactions. We benchmarked our simulations with finite-temperature exact diagonalization[63] for a 4 × 4 site system. For typical values of the experimental parameters used in this work, we found that the auto-correlation time was short after thermalization, needing about ten measurements for the density–density correlations compared to the 5,000 measurements we performed. The short auto-correlation time was partially due to the metastability of the states in the long-range interacting system's Hilbert space. To avoid this, we thermalized 64 different seeds and averaged the results. When estimating the temperature of the solids, we set the boundary condition to open and included measured harmonic confinement in the simulation but did not include the local chemical potential disorder. For the phase diagram in Fig. 3e, we set the temperature to $T = 0.2V_0/k_B$ (0.3 nK), the system size to 20 by 20 sites and the boundary condition to open. In addition, we assumed that the chemical potential was flat with no harmonic confinement and no disorder. For all phases, we used the location of the peak of the structure factor as the order parameter, which we then compared with the location of the structure factor peak in the classical limit of no tunnelling. The simulation of the structure factor in Fig. 3f has the same conditions as the phase diagram, but we used the experimental uncertainty in tunnelling to determine the error bars. In simulations at lower temperatures, the location of the structure factor peak did not shift but only narrowed, allowing us to simulate the emerging phases down to $t/V_0 = 0.05$ for Fig. 3e.

Data analysis

All density correlation and structure factor data shown in this paper were computed for a square-box analysis region whose size ranged from 11 by 11 sites to 15 by 15 sites, resulting in a full $C_{\mathbf{d}}$ matrix of 23 by 23 sites to 31 by 31 sites depending on the particular dataset. We show $C_{\mathbf{d}}$ in the figures only within $|d_x|, |d_y| \leq 4$ sites because most of the ordering we studied decayed within four sites. We computed the connected density–density correlation instead of the disconnected one because we wanted to distinguish the classical solid with a static phase from a solid with an uncertain phase. If static chemical potential disorder were to pin the solids down to one of the static phases, we would no longer have seen a signal in the connected density–density correlation. The observed correlation decayed exponentially over distance, so we mainly used a logarithmic colour scale and connected the positive and negative logarithmic scales with a linear scale. We computed the structure factor from the connected density–density correlation matrix extracted from, typically, up to $|d_x|, |d_y| \leq 9$ sites. To obtain the diagonal structure factors shown in Figs. 3f and 4f, we integrated the structure factor perpendicular to the straight line (shown in Figs. 3d and 4d) with a Gaussian envelope centred on the straight line. The centre filling was calculated by finding the maximum filling ratio in a 6 by 6 box among shots with a certain filling range (40% to 45%) in the whole analysis region of 16 by 16 sites.

Solid temperature

We compared the density–density correlation measured experimentally with the results of a quantum Monte Carlo simulation to estimate the temperature of our system. For the stripe solid, we estimated the temperature to be 0.8 nK; for the chequerboard solid, we estimated the temperature to be 0.7 nK. We computed the critical temperature to be around 0.5 nK for the stripe solid and estimated the critical temperature to be lower for the other types of solids examined in this work. To fix the particle density, we swept both the temperature and chemical potential, and then, for each temperature, we used the chemical potential that replicates the experiment's filling fraction in the central 16 sites. All solids in this paper exhibited a connected density–density correlation that decayed exponentially as we increased d, indicating that the system was above the critical temperature of the solids or that the chemical potential disorder and harmonic confinement were too large[57]. The exponential fits to the density correlations ($d > 1$) give the correlation length. Specifically, the stripe density–density correlation decayed exponentially with a correlation length of 2.22(5) sites for $\mathbf{d} = (d_x, 0)$ and 1.21(15) sites for $\mathbf{d} = (0, d_y)$. The chequerboard correlation decayed exponentially with a correlation length of 0.82(5) sites isotropically. The diagonal stripe correlation decayed with a correlation length of 0.6(2) along the diagonal directions. The observed correlations decayed exponentially in the experiment, but they were the same ones that were established at long range in the solid phases, and they can be observed in a whole subregion in some single-shot images (Fig. 2c).

Solid lifetime

After we ramped into the solid phases, we held the atoms for various durations and measured the overlap of the connected density–density correlation with the perfect solid correlation. We observed that overlap decayed roughly exponentially with a lifetime of 1 s for the stripe solid when the atomic dipole pointed along one lattice direction and 0.7 s for the chequerboard solid. The finite lifetime of our Wannier–Stark state in the vertical lattice as well as heating from technical sources like laser noise and scattering can contribute to the decay of the solid order. Such a lifetime enables future work that explores the phase transitions between dipolar quantum solids and supersolids, since such experiments require adiabatic ramps of the dipole orientation when the tunnelling energy is small.

Spontaneous symmetry breaking of stripe solids

Using the site-resolved single-shot images, we were able to examine the spontaneous symmetry breaking as we transitioned into a stripe solid. We chose a 2 by 6 site region in our system and studied the stripe ordering after postselection when there were exactly six atoms over these 12 sites. We defined a value that measures the distance of a single-shot image to the stripes of phases A and B (bottom of Extended Data Fig. 3a). With the simulated infinite temperature state, we saw that most of the values were centred between the two stripe patterns A and B, as the orange points show in Extended Data Fig. 3a. But in our experiment with the stripe solid, we observed the perfect stripe ordering more frequently, leading to a bimodal distribution. To demonstrate that there was no temporal correlation between the two stripe patterns and support the claim that the symmetry breaking was random, we calculated the auto-correlation of the stripe overlap values over different shots and demonstrated that the overlap value was stochastic with no auto-correlation peaks (Extended Data Fig. 3b). The above provides evidence that our stripe solid is a spontaneous symmetry-breaking state.

Data availability

The data that support the findings of this study are available from the corresponding authors on reasonable request.

55. Patscheider, A. et al. Determination of the scattering length of erbium atoms. *Phys. Rev. A* **105**, 063307 (2022).
56. Bloch, I., Dalibard, J. & Zwerger, W. Many-body physics with ultracold gases. *Rev. Mod. Phys.* **80**, 885–964 (2008).

57. Zhang, C., Safavi-Naini, A. & Capogrosso-Sansone, B. Equilibrium phases of dipolar lattice bosons in the presence of random diagonal disorder. *Phys. Rev. A* **97**, 013615 (2018).
58. Korbmacher, H., Domínguez-Castro, G. A., Li, W.-H., Zakrzewski, J. & Santos, L. Transversal effects on the ground state of hard-core dipolar bosons in one-dimensional optical lattices. *Phys. Rev. A* **107**, 063307 (2023).
59. Aeppli, A. et al. Hamiltonian engineering of spin–orbit-coupled fermions in a Wannier–Stark optical lattice clock. *Sci. Adv.* **8**, eadc9242 (2022).
60. Glück, M., Kolovsky, A. R. & Korsch, H. J. Lifetime of Wannier–Stark states. *Phys. Rev. Lett.* **83**, 891–894 (1999).
61. Li, T. C., Kelkar, H., Medellin, D. & Raizen, M. G. Real-time control of the periodicity of a standing wave: an optical accordion. *Opt. Express* **16**, 5465–5470 (2008).
62. Sadoune, N. & Pollet, L. Efficient and scalable path integral Monte Carlo simulations with worm-type updates for Bose–Hubbard and XXZ models. *SciPost Phys.* https://doi.org/10.21468/SciPostPhysCodeb.9 (2022).
63. Weinberg, P. & Bukov, M. Quspin: a Python package for dynamics and exact diagonalisation of quantum many body systems. Part I: spin chains. *SciPost Phys.* https://doi.org/10.21468/SciPostPhys.2.1.003 (2017).

Acknowledgements We wish to acknowledge V. Kaxiras, A. Kale, M. Xu, M. Sohmen, M. Mark and Y. Bao for help on building the experiment. We wish to acknowledge R. Sahay, B. Capogrosso-Sansone, E.-A. Kim, L. Homeier, A. Bohrdt, F. Grusdt, M. Lebrat, T. Esslinger, M. Kebric, S. Sachdev and C. A. R. Sa de Melo for helpful discussions. We are supported by the US Department of Energy Quantum Systems Accelerator (grant no. DE-AC02-05CH11231), the National Science Foundation (NSF) Center for Ultracold Atoms (grant no. PHY-1734011), the Army Research Office Defense University Research Instrumentation Program (W911NF2010104), the Office of Naval Research Vannevar Bush Faculty Fellowship (N00014-18-1-2863) and the Defense Advanced Research Projects Agency Optimization with Noisy Intermediate-Scale Quantum devices (W911NF-20-1-0021). A.D. acknowledges support from the NSF Graduate Research Fellowship Program (grant no. DGE2140743). The computations in this paper were run on the FASRC Cannon cluster supported by the FAS Division of Science Research Computing Group at Harvard University.

Author contributions L.S., A.D., M.S., R.G., S.F.O., A.K., A.H.H., G.A.P., S.E., S.D. and O.M. contributed to building the experiment set-up. L.S., A.D., M.S. and O.M. performed the measurements and analysed the data. A.D. performed the theoretical analysis. M.G. conceived the experiment in collaboration with F.F. M.G. supervised all works. All authors discussed the results. L.S., A.D., M.S., R.G., S.F.O., F.F., O.M. and M.G. contributed to the manuscript.

Competing interests M.G. is a cofounder and shareholder of QuEra Computing. All other authors declare no competing interests.

Additional information

Correspondence and requests for materials should be addressed to Lin Su or Markus Greiner.

Peer review information *Nature* thanks Blair Blakie and the other, anonymous, reviewer(s) for their contribution to the peer review of this work.

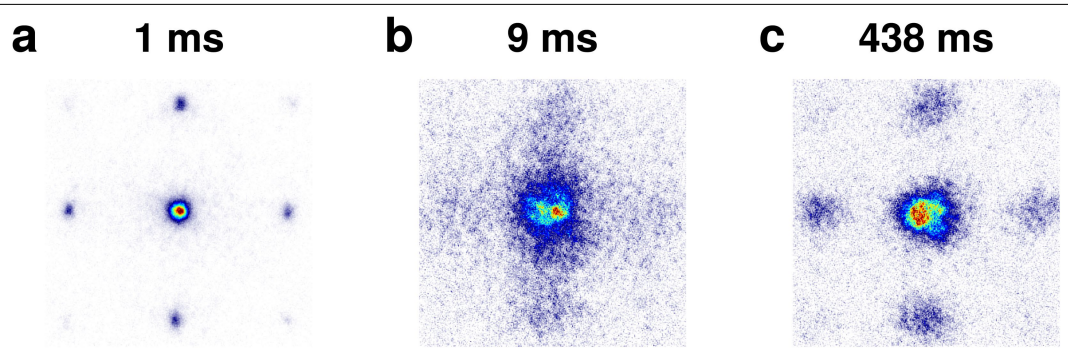

Extended Data Fig. 1 | Adiabaticity of the lattice ramp. We probe the adiabaticity of the lattice ramp by varying the duration as we follow the solid and dashed arrow to return to the star position at 7 E_R in Fig. 1d. When the ramp duration is very short at 1 ms (**a**), we see sharp coherence peaks in the time-of-flight image. As we slow down the ramp to a duration of 9 ms (**b**), the coherence peaks in the time-of-flight image are the least resolved. Further increasing the ramp duration up to 438 ms (**c**), we observe well-resolved coherence peaks again. The peaks are less sharp compared to those in **a**, possibly due to the decoherence and atom loss during the ramps, which in total takes almost 900 ms. These averaged images demonstrate that, with the ramp duration on the order of 100 ms in this paper, the system is in the adiabatic regime.

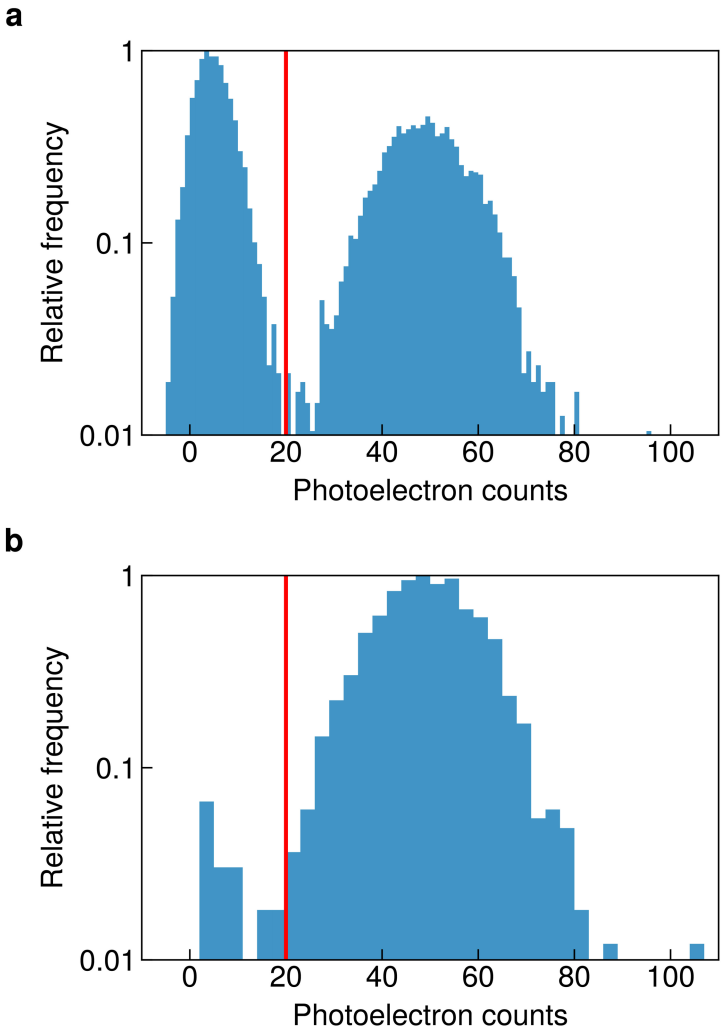

Extended Data Fig. 2 | Histogram for digitization of occupation number. We perform high-fidelity site-resolved imaging after expanding the 2D accordion lattice to 3 μm spacing. **a**, half-filling histogram. The fidelity to distinguish between 0 and 1 filling per site after expanding the 2D accordion lattice is more than 99%. **b**, unity-filling histogram. The efficiency of transferring atoms to the 2D accordion lattice and expanding is more than 98%.

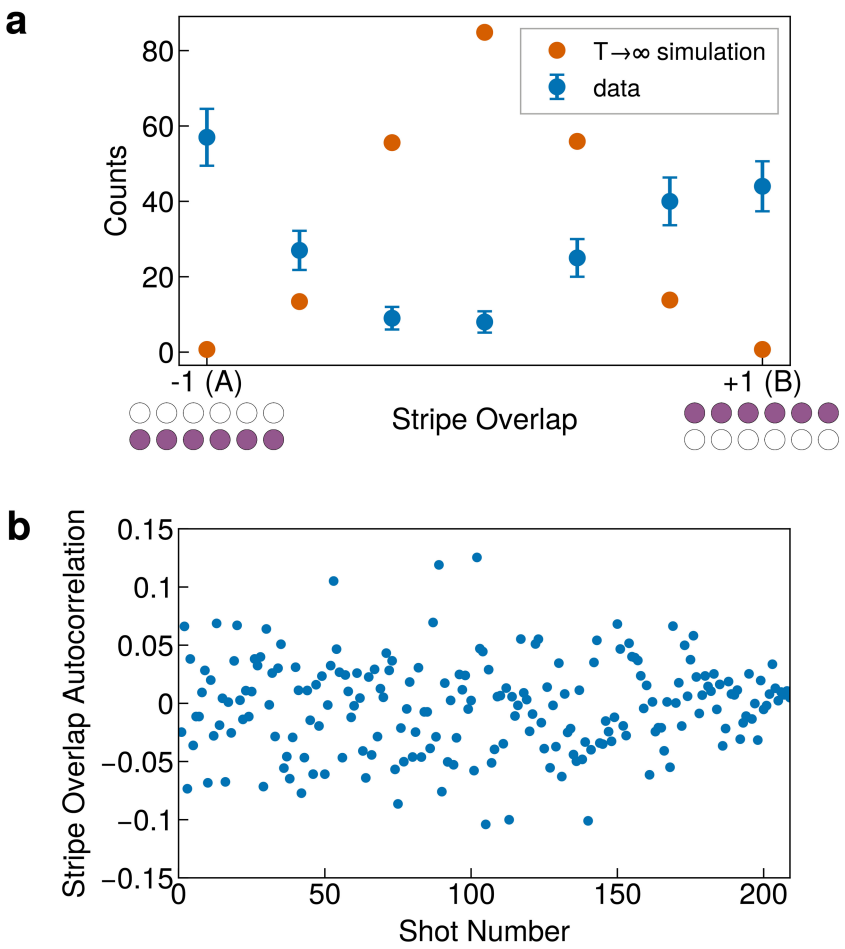

Extended Data Fig. 3 | Stripe overlap in a 2 by 6 box. We demonstrate the bimodal distribution of the macrostate that is temporally uncorrelated. **a**, histogram of the overlap of the stripe order with the single shot data (blue) and simulation of the infinite temperature state (orange). **b**, Auto-correlation of the stripe overlap data.